# Metal-facilitated, sustainable nitroarene hydrogenation under ambient conditions

Chongyan Ruan<sup>1‡</sup>, Kunran Yang<sup>1‡</sup>, Caitlin Beckett<sup>1</sup>, William Martin<sup>1</sup>, Eric D Walter<sup>2</sup>, Wenda Hu<sup>2</sup>. Junchen Liu<sup>1</sup>, Noha Zayan<sup>1</sup>, Benjamin Lessin<sup>1</sup>, Jacob Ken Faherty<sup>1</sup>, Ryota Akutsu<sup>3</sup>, Jian Zhi Hu<sup>2</sup>, and Fanxing Li\*<sup>1</sup>

**Abstract**: Hydrogenation is a critical reaction in the chemical industry, yielding a range of important compounds such as fine chemicals, pharmachemicals and agrochemicals. However, conventional hydrogenation typically requires pressurized hydrogen, high temperatures and involves noble metal catalysts. We proposed a two-step hydrogenation process, utilizing water as the hydrogen source for the industrially important reduction of nitroarenes to anilines. A metal or reduced metal oxide, which can be obtained from solar thermal or electrochemical reduction, acts as the active site for nitrobenzene adsorption, H<sub>2</sub>O dissociation and *in-situ* hydrogen generation. Among the 15 metal and reduced metal oxides investigated, Zn and Sn emerged as highly efficient catalysts for the reduction of a broad range of organic nitro compounds under mild conditions, with H<sub>2</sub> utilization efficiency 1-2 orders of magnitude above the state-of-the-art. The presented protocol provides extra dimensions for designing and optimizing conventional hydrogenation

<sup>&</sup>lt;sup>1</sup> Department of Chemical and Biomolecular Engineering, North Carolina State University, Raleigh, NC 27606, United States.

<sup>&</sup>lt;sup>2</sup> Institute for Integrated Catalysis and Earth and Biological Science Directorate, Pacific Northwest National Laboratory, Richland, Washington 99354, United States.

<sup>&</sup>lt;sup>3</sup> Chemistry and Materials Division, Department of Textile Science and Technology, Shinshu University, 3-15-1 Tokida, Ueda-shi, Nagano-ken, Japan, 386-8567.

<sup>\*</sup>These authors contributed equally: Chongyan Ruan, Kunran Yang

<sup>\*</sup>Corresponding Authors: fli5@ncsu.edu

process with an alternative pathway. The reactive hydrogen atoms generated in-situ effectively

overcome the barriers associated with hydrogen gas dissolution and its subsequent dissociation on

the catalyst surface, thereby greatly enhancing the overall effectiveness for the hydrogenation

reaction. This research potentially establishes a sustainable, generally applicable alternative to

conventional hydrogenation methods, simultaneously presenting a viable solution for renewable

energy storage.

**Keywords:** Nitroarenes; H<sub>2</sub>O splitting; *in-situ* hydrogenation; renewable energy storage

2

#### 1. Introduction

The chemoselective hydrogenation of aromatic nitro compounds to their corresponding functionalized anilines holds significant scientific and technological value from its original discovery over 150 years ago, since these anilines are crucial intermediates for a variety of products, including pharmaceuticals, agrochemicals, dyes, pigments, and others.[1-3] While traditional processes employing Fe/HCl generate large amounts of undesirable waste, catalytic hydrogenation using molecular hydrogen in the presence of a heterogeneous catalyst is well-established, and often the preferred method. However, selectivity problems in the presence of other common functional groups require carefully selected and expensive noble metal catalysts such as Au[4, 5], Pd[6], Pt[7, 8], or Ru[9], which are essential for H<sub>2</sub> activation and the subsequent hydrogenation. Switching from these noble metal catalysts to inexpensive non-noble metal catalytic systems is challenging. Meanwhile, catalytic hydrogenation is typically operated with a high H<sub>2</sub> pressure (3-60 bar) in large excess of the stoichiometrically specified amount due to the poor hydrogen solubility in most reaction mediums (1.6 mg/L in H<sub>2</sub>O, 2.5 mg/L in Phenol, 6.9 mg/L in Benzene, 8 mg/L in Ethanol, 1 atm and 25 °C)[10]. In addition to safety concerns, the large carbon footprint and high infrastructure costs associated with conventional hydrogenation have resulted in a growing interest in the reduction of nitroarenes under safer and eco-friendly conditions. As an alternative to molecular hydrogen, liquid organic hydrogen donors including hydrazine[11, 12], formic acid[13, 14], sodium borohydride[15], boranes, ammonia borane[16-19] and silanes[20] have been investigated. Despite the potential for selective chemoselectivity in nitro reduction, the use of these reducing agents still poses significant challenges such as toxicity and difficulty in their extraction from the reaction mixture. As a result, their usage is largely limited to laboratory scale organic synthesis. As an eco-friendly hydrogen generation approach, water splitting with renewable energy

has been extensively investigated in recent decades. For instance, solar fuel production *via* two-step thermochemical H<sub>2</sub>O splitting (STWS) taps sunlight for renewable H<sub>2</sub> generation[21-26], representing an attractive alternative to artificial photosynthesis and photovoltaic-driven electrolysis given its potential for higher efficiency[27]. However, despite the extensive research efforts in developing advanced water-splitting materials and efficiency improvement since the 1970s[28, 29], their application is still largely limited to hydrogen and/or CO generation through the splitting of water and/or CO<sub>2</sub>[30-34]. The potential of STWS for chemical production is still largely untapped. For instance, STWS can potentially deliver and/or incorporate hydrogen into a reactant molecule that would otherwise be achieved through a conventional hydrogenation process, although molecular H<sub>2</sub> does not need to be directly involved in the STWS-based hydrogenation reactions[35].

Aiming at a more efficient and sustainable process, we proposed and validated a two-step solar thermochemical/electrochemical hydrogenation (ST/ECH) approach, sourcing hydrogen directly from water to drive hydrogenation or reduction reactions. As illustrated in Fig. 1, during the hydrogenation step, an inexpensive metal or oxygen deprived metal oxide provides the active surface for reactants adsorption and a bulk source of reducing potential for H<sub>2</sub>O splitting as well as *in-situ* hydrogen generation. Meanwhile, the reactive H atoms generated *in situ* readily facilitate the reduction of adsorbed reactants and intermediates, thereby promoting the kinetics of the reaction while improving its thermodynamic favorability. During the regeneration step, the lattice oxygen can be abstracted from the reoxidized metal oxide through well-established electrochemical reduction using renewable electricity or solar thermochemical reduction driven by concentrated solar energy. ST/ECH provides a sustainable alternative for conventional hydrogenation techniques, representing an efficient method for harvesting and storing solar energy

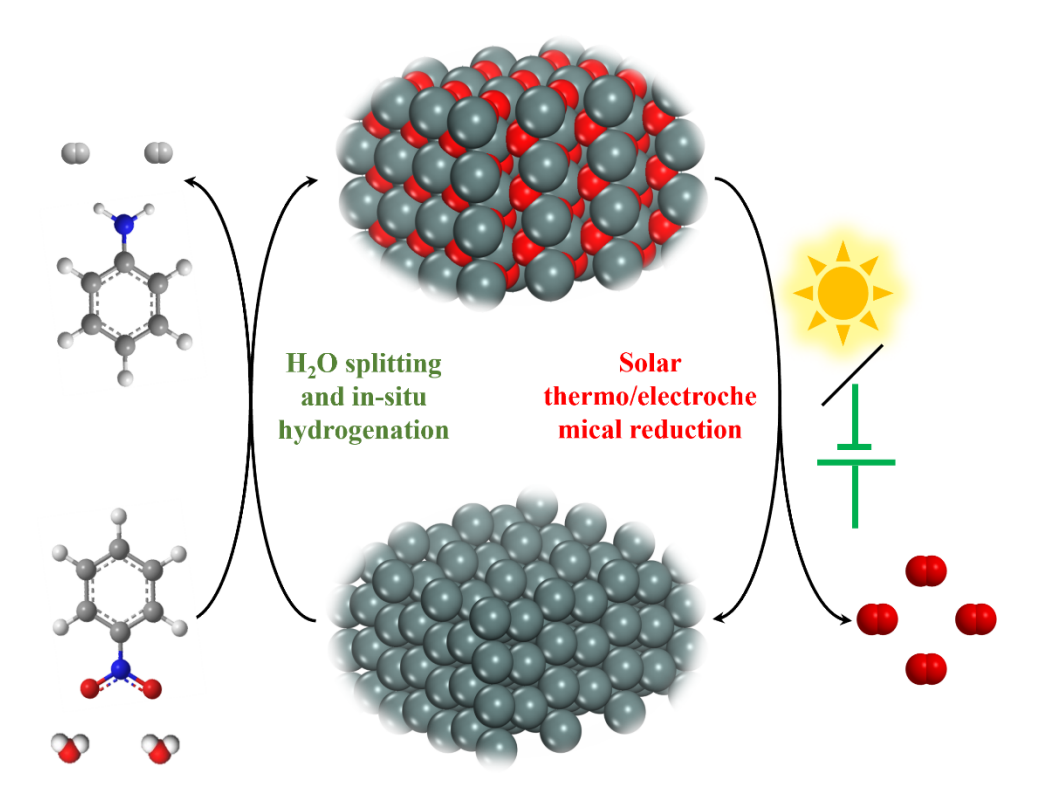


Fig. 1 Schematic of the two-step solar thermochemical/electrochemical hydrogenation (ST/ECH) process for aromatic nitro compounds hydrogenation. Colour code: Metal (dark cyan), O (red), C (dark grey), N (blue) and H (white).

via hydrogenation of aromatic nitro with the following inherent advantages: (i) ST/ECH has the potential to provide the reduction potential for a variety of reductive transformations without relying on molecular H<sub>2</sub> or organic hydrogen donors; (ii) ST/ECH introduces alternative mechanistic pathways other than those based on the conventional catalytic hydrogenation. The reactive atomic hydrogen is derived from *in situ* hydrogen generation on a metal or reduced metal oxide surface through H<sub>2</sub>O splitting rather than the dissociative cleavage of H<sub>2</sub>. Therefore, the barriers for H<sub>2</sub> dissolving in the reaction medium and the subsequent dissociation at the catalyst surface are eliminated. Thus, reactions that require high temperatures and pressures in conventional catalytic systems may readily occur at ambient temperatures and pressures; (iii) On

one hand, the electron-withdrawing nitro group tends to preferentially adsorb on the nucleophilic site of the metal/reduced metal oxide surface. On the other hand, the amine product, which exhibits a high affinity towards metal catalyst but less towards metal oxides, can be effectively desorbed promoted by the configuration change (metal to metal oxide), i.e., the oxidation of the metal catalyst during H<sub>2</sub>O splitting. This can in turn potentially promote nitroarenes conversion and amine formation; (iv) Employing metal/reduced metal oxide with different oxophilicities or by controlling the reduction extent of the metal oxide during regeneration, the reducing potential for H<sub>2</sub>O dissociation and the subsequent hydrogenation can be manipulated. This provides extra dimensions in modifying the activity and selectivity; (v) Under ST/ECH conditions, the only byproduct is O<sub>2</sub>, leading to an atom-economic transformation process which is essentially wastefree.

Herein, the hydrogenation of nitrobenzene is chosen as a model reaction to evaluate the proposed ST/ECH process. The current work concentrates on the unique hydrogenation step since the reduction half cycle of various redox active oxides has been well-documented for commercial production of metals[36, 37], solar-thermochemical H<sub>2</sub>O or CO<sub>2</sub>-splitting[22, 24, 30, 38], and chemical looping[39-42]. 14 oxophilic zero-valent metals including Zn, Sn, Al, Ti, Mg, Mn, Fe, Mo, V, Ga, Cr, W, In and AlCuZn alloy as well as non-stoichiometric CeO<sub>2-δ</sub> were employed as prototype catalysts to investigate the feasibility of this process. Remarkably, selective reduction of a wide range of organic nitro compounds were achieved at ambient temperature and pressure over Zn and Sn catalysts, with an unparalleled H<sub>2</sub> utilization efficiency that is 1-2 orders of magnitude higher than state-of-the-art catalytic hydrogenation processes. Mechanistic investigations via combined experimental and theoretical studies indicate that zero-valent metals or surface oxygen vacancies are active redox sites for *in-situ* generation of H atoms from H<sub>2</sub>O and the subsequent

reduction of nitroarenes. With its promising generalizability, the ST/ECH process can open new avenues for the storage of renewable energy via a myriad of organic transformations without using fossil derived H<sub>2</sub>.

#### 2. Experimental Section

#### 2.1. Materials

Nitrobenzene (99%), Nitrosobenzene (Analytical standard, ≥99.9%), N-Phenylhydroxylamine (Analytical standard, ≥99.9%), Aniline (BioRenewable, anhydrous, ≥99%, inhibitor-free), 4-Fluoroaniline (≥98,5%), 1-Fluoro-4-nitrobenzene (≥98,5%), 4-Chloroaniline (Analytical standard, ≥99.9%), 1-Chloro-4-nitrobenzene (Certified, ≥99.9%), 1-Br-3-nitrobenze (≥97.5%), 3-Bromoaniline (≥97.5%), 3-Nitrophenol (Reagentplus, 99%), 3-Aminophenol (99%), 4-Nitrotoluene (≥98.5%), 4-Aminotoluene (≥98.5%), 4-Nitrobenzaldehyde (99%), 4-Aminobenzaldehyde (99%) were of analytical grade and purchased from Sigma-Aldrich. 4-Nitrophenylacetylene (97%) and 4-Ethynylaniline (97%) were purchased from ThermoFisher Scientific.

#### Catalyst Preparation

Zn (nanopowder, 40-60 nm avg. part. size, ≥99% trace metals basis), Sn (nanopowder, <150 nm particle size (SEM), ≥99% trace metals basis), Ti (powder, -325 mesh, 99.5% trace), Mg (powder, ≥99% trace metals basis), Mn (powder, -325 mesh, ≥99% trace metals basis), Fe (≥99%, power (fine)), Mo (powder, 1-5 µm, 99.9% trace), V (powder, -325 mesh, ≥99.5% trace metals basis), Ga (99.9995% trace metals basis), Cr (powder, 99.5%, −100 mesh), W (≥99%, fine powder), In (powder, −60 mesh, 99.999% trace metals basis), Devardas' alloy (AlCuZn, Al (44-46%), Cu (49-

51%), Zn (4-6%), powder, -100 mesh) were purchased from Sigma-Aldrich. Al (powder, -325 mesh, 99.5% trace) was purchased from Alfa Aesar. All the chemicals were used without further treatment. CeO<sub>2</sub> (99.9%) was purchased from Noah Technologies Corporation. Prior to the experiment, the as-received CeO<sub>2</sub> was reduced in 10% H<sub>2</sub>/Ar (100 mL/min) at 800 °C for 2 h.

#### 2.2. Catalyst Characterization

X-ray powder diffraction (XRD) patterns were collected at room temperature on a Rigaku SmartLab X-ray diffractometer equipped with Cu K $\alpha$  X-ray radiation (45 kV, 40 mA,  $\lambda$  = 1.5418 Å). Diffraction profiles were collected in the  $2\theta$  range of  $10-80^{\circ}$  with a step size of  $0.02^{\circ}$  and a counting time of 40s/step. Phase identification and quantification were conducted based on whole pattern fitting using Rietveld refinement with the PANalytical X'Pert HighScore Plus software. Surface morphology of the catalyst was investigated on a ThermoFisher Verios 460L Field Emission scanning electron microscopy (SEM) operated at 2 kV. Samples for electron microscopic studies were adhered directly to conductive carbon tape and secondary electron images were collected without any coating. Excess powder was removed by gently blowing with a nozzle. Highresolution transmission electron microscopy (HRTEM) was performed on a FEI Titan 80-300 transmission electron microscope, which was equipped with a liquid nitrogen cooled energydispersive X-ray spectroscopy (EDX) detector for elemental analysis under a working voltage of 200 kV. All samples were crushed into fine powders and dispersed in ethanol by ultrasonication. The suspension was then drop casted onto a holey-carbon coated Cu grid and dried in air under ambient conditions. Diffuse reflectance infrared Fourier transform (DRIFT) spectra were performed on a Thermo Scientific Nicolet iS50 FT-IR spectrometer in a Pike DiffusIR cell equipped with a KBr window. Typically, samples were homogenously blended with KBr in a

weight ratio of 1:3 and loaded in the alumina crucible. Pretreatment up to 100 °C in flowing Ar (30 mL/min) was performed to remove physically adsorbed H<sub>2</sub>O and gases, mainly carbon dioxide. The sample was then cooled down to 25°C and a spectrum was collected and used as a background for the following measurements. An Ar carrier gas (30 ml/min) saturated with nitrobenzene vapor at room temperature was introduced to the cell for 60 min, followed by purging with Ar for another 60 min at 30 ml/min to remove gaseous and physically adsorbed molecules. The FT-IR spectra were measured at room temperature, accumulating 64 scans with a resolution of 4 cm<sup>-1</sup>. EPR experiments were performed on a Bruker Elxsys X-band spectrometer equipped with an SHQe resonator. Samples were contained in flame sealed quartz tubes (2mm OD x 1mm ID), typically consisting of 0.5 mg catalyst, 1 ul of nitrobenzene and 10 ul of water. The magnetic field was modulated 0.5 G and swept 75 G in 10 s with 10 scans averaged. Microwave power was 2 mW at a typical frequency of 9.32 GHz, and a time constant of 0.041 s was employed.

#### 2.3. Typical Procedure for the Catalytic Evaluation

Catalytic reactions were conducted in a 50 mL stainless-steel autoclave fitted with a Teflon liner (Parr 4579). The reaction was carried out at 25-150 °C for 4h at a stirring speed of 400 rpm. (i) For a typical nitrobenzene hydrogenation with H<sub>2</sub>O as the hydrogen donor, the reactor was loaded with nitrobenzene (1 mmol, 102 µL), redox catalyst (0.4 g) and de-ionized water (15 ml). Prior to the heating, the reactor was flushed with inert Ar (>99.999%, Air gas) six times to remove the Air, charged with Ar at 1 atm in absence of hydrogen. (ii) For conventional nitrobenzene hydrogenation reactions with H<sub>2</sub>, the reactor was charged with 1 mmol of nitrobenzene, 0.4 g of catalyst and 15 ml of de-ionized water. After being purged with H<sub>2</sub> (>99.999%, Air gas) six times, the reactor was pressurized to 2 MPa with H<sub>2</sub> and heated to the set temperature subsequently. After reaction and

cooling to room temperature, the reactor was depressurized and the products were filtered and analyzed.

The reaction products were analyzed by online gas chromatograph (Agilent model 7820A) equipped with a flame ionization detector (FID) and an J&W DB-5 GC Column (30 m, 0.25 mm, 0.25 μm, 7 inch cage) using an external standard method. The products were identified by gas chromatograph—mass spectrometry (GC–MS) using an Agilent 7820 GC equipped with an HP-1 MS capillary column (100% dimethylpolysiloxane), and also by comparison with commercially pure products. The accuracy of the measurement was assured by performing carbon balances. The carbon balance was 90-105%.

Carbon balance: moles of C measured in the reactor effluent = mole of C in the feedstock (1)

The Nitrobenzene conversion and product selectivity are calculated as follows:

$$Nitrobenzene conversion = \frac{\text{Moles of product in the reactor effluent}}{\text{Mole of nitrobenzene in the feedstock}}$$
 (2)

Product selectivity = 
$$\frac{\text{Moles of product produced}}{\text{Mole of nitrobenzene consumed}}$$
 (3)

For nitrobenzene hydrogenation with H<sub>2</sub>O as the hydrogen donor, the hydrogen utilization efficiency is defined as the molar ratio of hydrogen consumed to produce the hydrogenated products per amount of hydrogen produced. The latter is determined by the extent of oxidation of the redox catalyst based on Rietveld refinement of XRD spectra. Using Zn as an example:

$$\label{eq:hydrogen} \text{Hydrogen utilization efficiency} = \frac{\sum_{i=1}^{n} n_i * a_i}{\text{Initial Zn^0 amount} - \text{Zn^0 amount after reaction}}$$

$$= \frac{\text{Moles of H}_2 \text{ consumed}}{\text{Moles of H}_2 \text{ Prodcued}} \tag{4}$$

where n<sub>i</sub> donates the mole amount of the hydrogenation product i; a<sub>i</sub> donates the stoichiometric coefficient of the corresponding hydrogenation reaction. All the parameters in the above equation are expressed in a H<sub>2</sub>-equivalent basis, even though atomic hydrogen is consumed for the hydrogenation reactions in the STCH process.

For conventional nitrobenzene hydrogenation reactions with H<sub>2</sub>, the hydrogen utilization efficiency can be evaluated as:

$$H_2$$
 utilization efficiency =  $\frac{\sum_{i=1}^{n} n_i * a_i}{nH_2}$  (5)

where nH<sub>2</sub> donates the total amount of H<sub>2</sub> charged in the reactor and can be calculated using the ideal-gas equation of state.

#### 2.4 . Computational details

The DFT calculations were performed by using Vienna ab initio simulation package (VASP) software.[43] The generalized gradient approximation (GGA) method combined with the projector-augmented wave (PAW) method were employed to calculate the electronic structures and the corresponding electron-core interaction, respectively.[44] Here we chose the Perdew-Burke-Ernzerhof (PBE) functional with the cutoff energy 450 eV and force convergence criterion of 0.05 eV Å<sup>-1</sup>.[45] The lattice parameters of Zn and ZnO were fully optimized; 3-layer 5×5 Zn(001) and 3×2 ZnO(1010) supercell slabs were built with the bottom layer of atoms fixed and the upmost two layers of atoms and the adsorbates were relaxed during all of the calculations. The ZnO/Zn structure was built by placing extra ZnO clusters onto Zn(001) and, the resulting structure underwent thorough optimizations to obtain a stable structure. The vacuum layer was larger than 12 Å. The structures have x and y dimensions larger than 10 Å, and all of the calculations were performed by 2 × 2 × 1 k-point grid. The transition-state structures were obtained by climbing

image nudged elastic band (CI-NEB).[46] Vibrational frequency calculations were performed to characterize the transition state structures and also to calculate the zero-point energies. Solvent effects significantly affect the reaction activity,[47, 48] thus here we used the implicit solvation models by VASPsol to involve the solvation effect into the calculations.[49]

The definition of adsorption energy ( $E_{ads}$ ) and reaction energy ( $\Delta E$ ) is defined as below and we added more description correspondingly.

$$E_{\text{ads}} = E_{\text{slab+species}} - E_{\text{slab}} - E_{\text{species}} \tag{6}$$

$$\Delta E = E_{\text{products}} - E_{\text{reactants}} \tag{7}$$

where  $E_{\text{slab+species}}$  indicates the total energy of the system with the species adsorbed on the surface,  $E_{\text{slab}}$  means the energy of the surface structure,  $E_{\text{species}}$  represents the energy of the species in a system without the surface structure,  $E_{\text{products}}$  and  $E_{\text{reactants}}$  denote the energy of products and reactants in each reaction, respectively.

#### 3. Results and Discussion

**3.1 Redox Performance.** The feasibility of ST/ECH depends largely upon the thermodynamic and kinetic properties of the redox catalysts. Therefore, the reduced metal or metal oxides must be thermodynamically favorable for H<sub>2</sub>O splitting. Meanwhile, their oxidized counterparts need to be easily reducible either thermochemically or electrochemically. The H<sub>2</sub>O splitting (per 2 mol of H<sub>2</sub>), and thermal regeneration of the metal oxide (per mol of O<sub>2</sub>) can be exemplified as follows:

$$Metal + 2H_2O = Metal \text{ oxide} + 2H_2(g)$$
(8)

$$Metal oxide = Metal + O_2(g)$$
 (9)

Take Zn as an example:

$$2Zn+2H_2O=2ZnO+2H_2(g)$$
 (10)

$$ZnO=Zn+O_{2}(g)$$
 (11)

Fig. 2a shows the thermodynamic potentials of water splitting for 19 metal/metal oxide and 1 reduced metal oxide/metal oxide redox pairs versus temperature. The  $\Delta G_{rxn}$  with temperature for regeneration of the corresponding metal oxides are plotted in Fig. S1. The  $\Delta G_{rxn}$  curves plotted in Fig. 2a<sub>1</sub>, a<sub>2</sub> indicate that H<sub>2</sub>O splitting is thermodynamically feasible ( $\Delta G_{rxn} < 0$  or small) with Mo, Sn, Fe, W, In, CeO<sub>1.83</sub>, V, Zn, Ga, Cr, Mn, Ti, Al and Mg from 0-300 °C. Whereas Ag, Rh, Cu, Bi, Co, and Ni are not able to split H<sub>2</sub>O spontaneously at this temperature range, which means a work input equal to the  $\Delta G_{rxn}$  at the water splitting temperature is necessary to drive the reaction. In the preliminary catalyst screening, 14 potential candidates including Zn, Sn, Al, Ti, Mg, Mn, Fe, Mo, V, Ga, Cr, W, In and Devarda's Alloy (AlCuZn) as well as non-stoichiometric CeO<sub>2-δ</sub> were tested for the industrially important nitrobenzene hydrogenation (Fig. 2b and Fig. S2). Among the different metals investigated, Zn and Sn exhibited significant activity. As shown in Fig. 2b<sub>1</sub>, a high nitrobenzene conversion (83%) was achieved over Zn even at room temperature (25 °C), giving nitrosobenzene (12.7%), N-Phenylhydroxylamine (60.4%), and aniline (26.9%) as the primary products. Selectivity for aniline increased with increasing reaction temperature, accompanied by a decreased nitrosobenzene and N-Phenylhydroxylamine selectivity (Fig. 2b<sub>1</sub>, b<sub>2</sub>). Upon further increasing the reaction temperature to 100 °C, a full conversion and complete selectivity to aniline for both Zn (Fig. 2b<sub>1</sub>) and Sn (Fig. 2b<sub>2</sub>) were obtained. The temperature-dependent selectivity suggests the activation barrier for the reduction of N-Phenylhydroxylamine to aniline may be higher than that for reduction of nitrobenzene (or nitrosobenzene) to N-Phenylhydroxylamine, allowing for a complete selectivity to aniline at a higher temperature. This will be further discussed in the mechanistic discussion section. The fact that no traces of reaction intermediates such as the azoxybenzene, azobenzene and hydrazobenzene were detected indicates that ST/ECH of

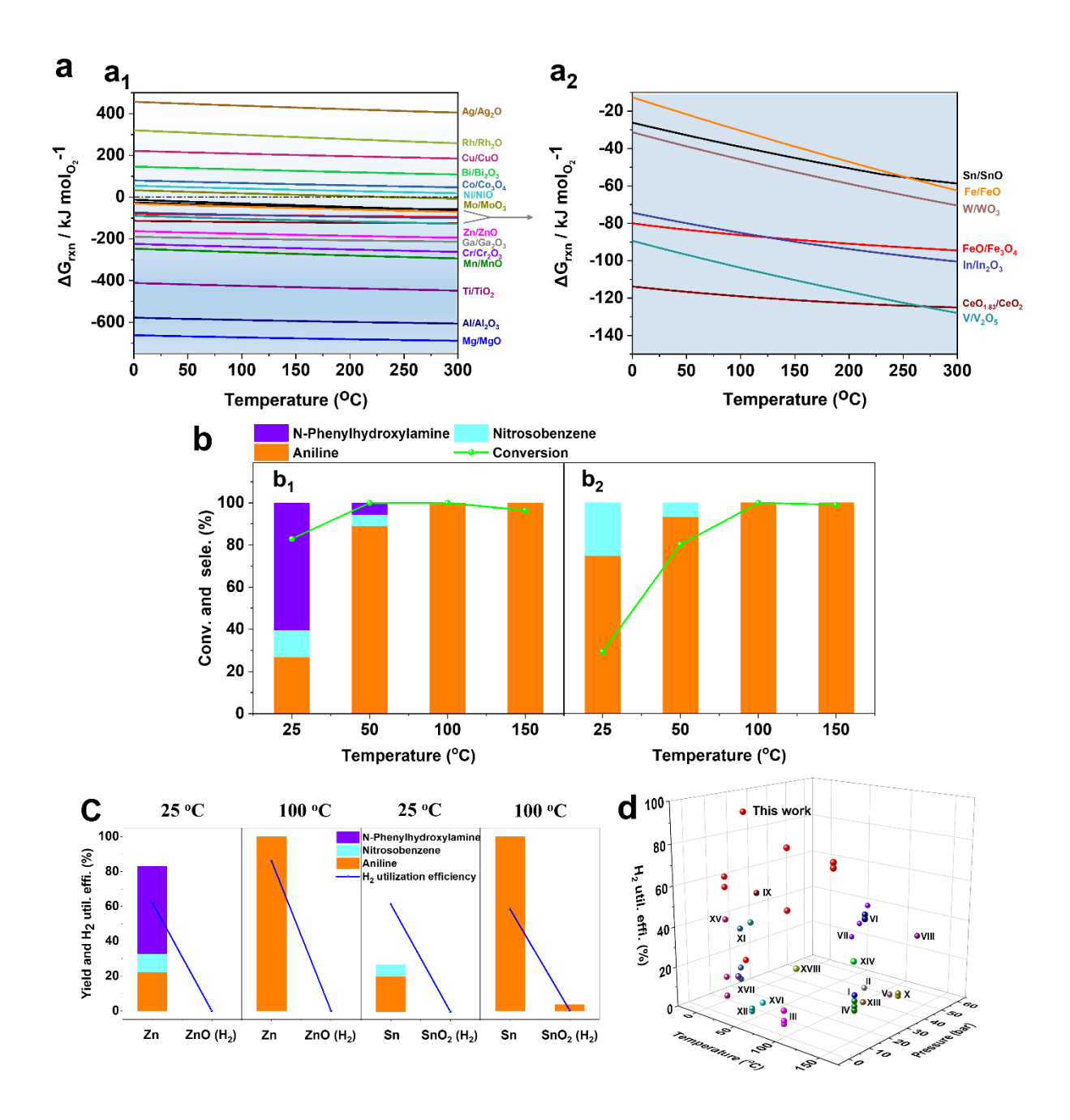


Fig. 2 (a) Gibbs free energy change ( $\Delta G_{rxn}$ ) of H<sub>2</sub>O splitting reaction over metal or reduced metal oxide (metal/reduced metal oxide + 2H<sub>2</sub>O  $\rightarrow$  metal oxide + 2H<sub>2</sub>) as a function of temperature at 1 bar. (b) Conversion and product selectivity for ST/ECH of nitrobenzene using (b<sub>1</sub>) Zn and (b<sub>2</sub>) Sn catalyst from 25-150 °C. Reaction conditions: 1mmol of nitrobenzene, 15 mL H<sub>2</sub>O and 0.4 g of catalyst, 4 h, 1 atm of Ar. (c) Product yield and H<sub>2</sub> utilization efficiency over Zn and Sn catalysts

for ST/ECH of nitrobenzene as compared with the conventional molecular-hydrogen-based hydrogenation process over ZnO catalyst (2 MPa H<sub>2</sub>) and SnO<sub>2</sub> catalyst (2 MPa H<sub>2</sub>) at 25 and 100 °C. Reaction conditions: 1mmol of nitrobenzene,15 mL H<sub>2</sub>O and 0.4 g of catalyst, 4 h, 1 atm of Ar or 2 MPa H<sub>2</sub>. (d) Comparison of hydrogen utilization efficiency for ST/ECH of nitrobenzene over Zn and Sn catalyst with the state-of-the-art catalysts employing molecular hydrogen or other organic hydrogen donors as the reducing agent. I, Jin et al.[50]; II. Long et al.[51]; III, Zhang et al.[52]; IV, Wei et al.[53]; V, Westerhaus et al.[3]; VI, Zhou et al.[54]; VII, Shi et al.[55]; VIII, Li et al.[56]; IX, Ryabchuk et al.[57]; X, Jagadeesh et al.[58]; XI, Zhu et al.[59]; XII, Zhang et al.[60]; XIII, Ye et al.[61]; XIV, Sorribes et al.[62]; XV, Cheruvathoor et al.[11], XVI, Gawande et al.[63]; XVII, Geilen et al.[64]., XVIII, Zhou et al.[54]. Refer to Table S2 for more details.

nitrobenzene is most likely to proceed through the direct pathway, even though the molecular hydrogen is not directly involved (see Scheme 1 in supplementary information). The kinetic profile of ST/ECH of nitrobenzene over Zn (Fig. S4a) and Sn (Fig. S4b) catalysts features complete nitrobenzene conversion and aniline selectivity from 0.5-8h at 100 °C, indicating rapid H<sub>2</sub>O spitting and nitrobenzene hydrogenation kinetics. Note that in conventional catalytic hydrogenation, Felix et al.[3] revealed that nitrobenzene was converted into aniline in 300 min over cobalt oxide catalysts on activated carbon, with near 100% conversion and selectivity (110 °C, 5 MPa of H<sub>2</sub>). Hongqiang et al.[65] showed that nitrobenzene was completely converted with >99% amine selectivity in 210 min over N/P dual-coordinated single atom cobalt catalyst (110 °C, 3 MPa of H<sub>2</sub>). Despite Al, Ti, Mg, Mn and Ga exhibit higher thermodynamic driving forces for H<sub>2</sub>O splitting as compared to Zn and Sn (Fig. 2a), comparatively lower nitrobenzene conversions and hydrogenation rates were observed at 25 and 100 °C (see Fig. S2 and Fig. S3 for more details). Reaction with Cr, W and In at 25 and 100 °C revealed no hydrogenated product at

all (Table S1, entries 1-6). This may be due to sluggish H<sub>2</sub>O splitting and nitrobenzene hydrogenation kinetics.

The amines product yield and H<sub>2</sub> utilization efficiency of Zn and Sn (defined as the molar ratio of hydrogen added to the hydrogenated products to the total amount hydrogen from water splitting based on the Zn or Sn consumed) for ST/ECH of nitrobenzene were further compared to the conventional molecular-hydrogen-based hydrogenation process over ZnO and SnO<sub>2</sub> at 25 and 100 °C. As illustrated in Fig. 2c, 29-100% amine yield was observed for ST/ECH of nitrobenzene over Zn (83% yield at 25 °C, 100% yield at 100 °C) and Sn (29% yield at 25 °C, 100% yield at 100 °C) using H<sub>2</sub>O as the hydrogen source. Meanwhile, superior hydrogen utilization efficiencies of 58.4-86.1% were achieved over Zn and Sn for ST/ECH of nitrobenzene (Fig. 2c, Fig. S5). The exceptional hydrogen utilization efficiency indicates that the nitrobenzene hydrogenation via water dissociation dominated the reaction pathway instead of the competing hydrogenation evolution reaction. And the in situ generated atomic H species are highly effective for nitrobenzene hydrogenation. In contrast, no appreciable reaction took place over ZnO, SnO<sub>2</sub>, Al<sub>2</sub>O<sub>3</sub>, and TiO<sub>2</sub> (0-7.4% aniline yield at 25 and 100 °C) via direct hydrogenation when the reaction was carried out under high pressure H<sub>2</sub> (Fig. 2c, Table S1, entries 7-14). These results indicate that water dissociation by metal catalysts was the key step for nitrobenzene hydrogenation and the direct participation of molecular hydrogen was largely limited. The hydrogen utilization efficiency was further compared to state-of-the-art catalysts employing molecular hydrogen or other organic hydrogen donors such as N<sub>2</sub>H<sub>4</sub>, HCOONH<sub>4</sub>, HCOOH and NH<sub>3</sub> BH<sub>3</sub> as the reducing agent (Fig. 2d, see Table S2 for more details). Notably, one to two orders of magnitude higher efficiency were achieved, demonstrating the great efficacy of the ST/ECH process. The small fraction of unconverted hydrogen cogenerated for ST/ECH of nitrobenzene is available for storage, used as a

**Table 1.** Summary of reaction performance for the two-step ST/ECH of nitroarenes to anilines over Zn and Sn. Reaction conditions: 4 h, 100 °C, 1 atm of Ar, 1mmol of nitroarene,15 mL H<sub>2</sub>O and 0.4 g of catalyst.

Entry	Catalyst	Substrate	Amine	Conv. (%)	Sele. (%)	Average reaction rate (mmol g <sup>-1</sup> h <sup>-1</sup> ) <sup>a</sup>
1	Zn	NO <sub>2</sub>	NH <sub>2</sub>	>99.9	42.5	1.51
2	Sn	NO <sub>2</sub>	NH <sub>2</sub>	>99.9	53.6	0.76
3	Zn	F NO <sub>2</sub>	F NH <sub>2</sub>	>99.9	70.8	1.51
4	Sn	CI NO <sub>2</sub>	CI NH <sub>2</sub>	>99.9	86.9	0.76
5	Zn	CI O <sub>2</sub> N Br	CI H <sub>2</sub> N Br	>99.9	83.9	1.51
6	Sn	O <sub>2</sub> N Br	H <sub>2</sub> N Br	>99.9	100	0.76
7	Zn	O <sub>2</sub> N OH	H <sub>2</sub> N OH	>99.9	93.7	1.51
8	Sn	O <sub>2</sub> N OH	H <sub>2</sub> N OH	>99.9	100	0.76
9	Zn	NO <sub>2</sub>	NH <sub>2</sub>	>99.9	85.4	1.51
10	Sn	NO <sub>2</sub>	NH <sub>2</sub>	>99.9	89.6	0.76
11	Zn			>99.9	92.8	1.51
12	Sn	02N	H <sub>2</sub> N	>99.9	98.0	0.76
13	Zn	O <sub>2</sub> N N <sub>2</sub> O	H <sub>2</sub> N	<sup>42</sup> >99.9	>99.9	1.51
14	Sn	N <sub>2</sub> 0	NF NF	·l <sub>2</sub> >99.9	>99.9	0.76

<sup>&</sup>lt;sup>a</sup>The Zn and Sn converted are based on the XRD Rietveld refinement before and after STC/EH of nitrobenzene.

fuel, or serve as a reducing reactant to further increase the process efficiency. To demonstrate the general applicability of this approach, a large number of substituted nitroarenes were examined.

Table 1 demonstrates that, even without further optimization, a wide variety of industrially relevant anilines, including chloro- and fluoroanilines, were produced with moderate-to-excellent yields (see entries 1–6). This approach also showed strong tolerance for other easily reducible substituents, such as the OH, -CHO and  $-C \equiv C-$  groups (Table 1, entries 7-8, entries 11-14).

3.2 Redox Catalyst Characterizations. To elucidate the underlying reasons for the exceptional efficacy of the metal catalysts, various physicochemical characterizations, complemented with DFT calculations, were carried out for in-depth understanding of the redox chemistry and potential reaction pathways. Fig. 3a, b shows the phase evolution of the Zn and Sn catalyst before and after ST/ECH of nitrobenzene in H<sub>2</sub>O from 25 to 150 °C. For the initial Zn (Fig. 3a) and Sn (Fig. 3b) catalysts, a two-phase mixture consisting of Zn (JCPDS 04-005-9306) and ZnO (JCPDS 01-080-3002) or Sn (JCPDS 04-016-6444) and SnO (JCPDS 04-008-7670) was observed, with a Zn percentage of 61.6 wt.% and a Sn percentage of 91.9 wt.% as determined by Rietveld refinement (Fig. S6). Note that this Zn content is comparable to those obtained from a pilot-scale solar reactor via thermal dissociation of ZnO using concentrated solar power (44 wt.%)[37]. Peaks characteristic of metallic Zn and Sn progressively decreased in intensity upon increasing the reaction temperature from 25-150 °C (see Fig. S7, Fig. S8, Table S3 and Table S4 for more details), due to the enhanced driving force for Zn and Sn oxidation with increasing reaction temperature. Diffraction peaks associated with metallic Zn and Sn almost completely disappeared after ST/ECH of nitrobenzene in H<sub>2</sub>O at 150 °C, with only traces of Zn (0.8% wt.%) and Sn (8.0% wt.%)

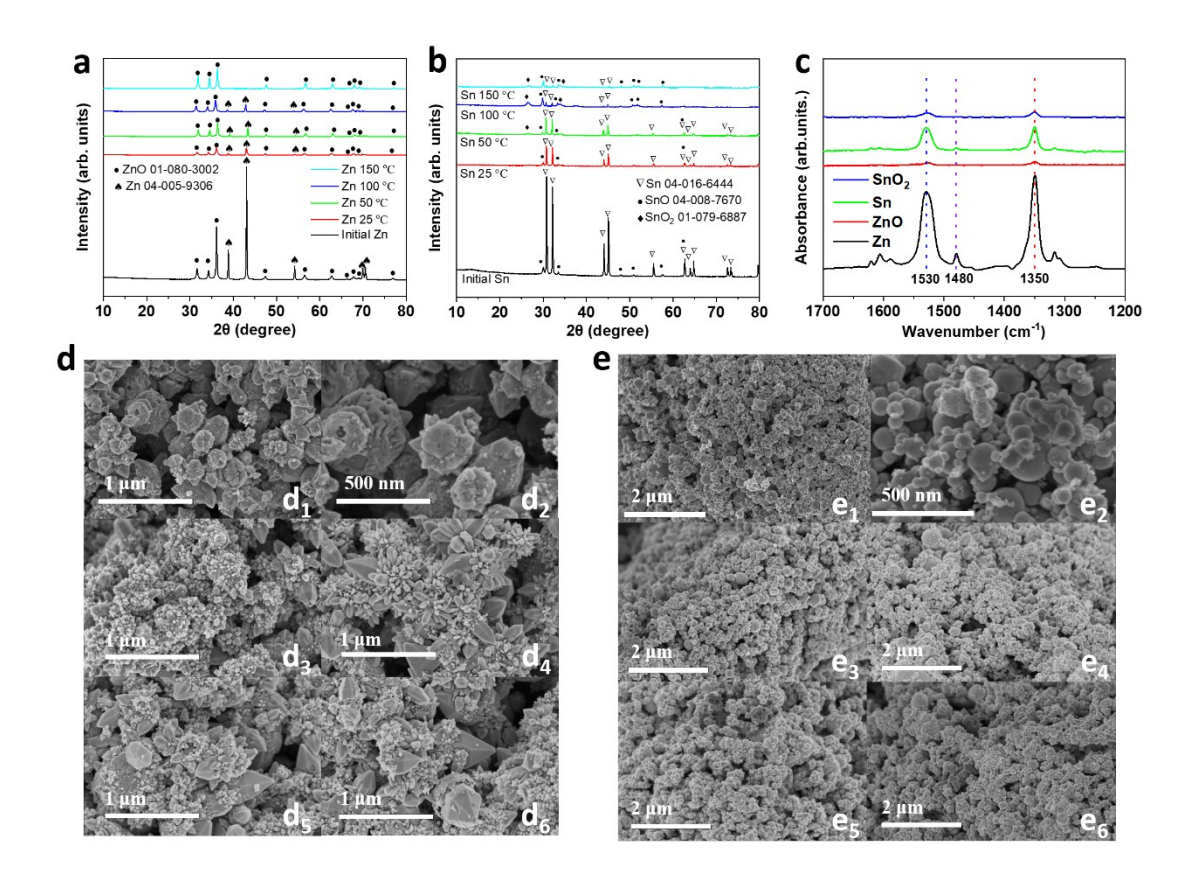


Fig. 3 X-ray powder diffraction patterns of (a) Zn and (b) catalyst before and after ST/ECH of nitrobenzene in H<sub>2</sub>O from 25 to 150 °C. (c) DRIFT spectra of nitrobenzene adsorption on Zn and ZnO, Sn and SnO<sub>2</sub> catalysts. Representative SEM images of Zn catalyst before (d<sub>1</sub>, d<sub>2</sub>) and after ST/ECH of nitrobenzene in H<sub>2</sub>O at (d<sub>3</sub>) 25 °C, (d<sub>4</sub>) 50 °C, (d<sub>5</sub>) 100 °C and (d<sub>6</sub>) 150 °C. Representative SEM images of Sn catalyst before (e<sub>1</sub>, e<sub>2</sub>) and after ST/ECH of nitrobenzene in H<sub>2</sub>O at (e<sub>3</sub>) 25 °C, (e<sub>4</sub>) 50 °C, (e<sub>5</sub>) 100 °C and (e<sub>6</sub>) 150 °C.

remaining, indicative of a near complete oxidation of Zn and Sn after reaction (Fig. S7, Fig. S8, Table S3 and Table S4). These results are in agreement with their superior nitrobenzene hydrogenation performance. The possible crystalline phase transition of Al, Ti, Mg, Mn, Fe, Mo, V, Cr, W, In and Devarda's Alloy (AlCuZn) as well as reduced CeO<sub>2</sub> after ST/ECH of nitrobenzene

were also investigated (see Fig. S9 and Fig. S10 for more details). Apart from the main metallic phases, traces of new reflections attributable to AlO(OH), Al(OH)<sub>3</sub> and Mg(OH)<sub>2</sub> are identified for Al (Fig. S9a) and Mg (Fig. S10a) after STC/EH of nitrobenzene. While for Ti (Fig. S9b, c), Fe (Fig. S10c, d), Mo (Fig. S10e, f), V (Fig. S10g, h) and Devarda's Alloy (AlCuZn) (Fig. S10i, j), no additional peak was observed after the nitrobenzene hydrogenation step. Careful inspections reveal that the corresponding peaks around 40-50 degrees shifted toward higher angles after the nitrobenzene hydrogenation step, with more notable shifts at higher reaction temperatures (Fig. S10d, f, h, j). These results suggest that the zero-valent Fe, Mo, V, and Devarda's Alloy (AlCuZn) are partially reoxidized. Meanwhile, the reoxidaion extents increase with increasing the reaction temperature. For reduced CeO<sub>2</sub> (Fig. S10k, 1), partial oxidation of the catalyst was revealed, evidenced by the peak shift as opposed to the emergence of new phases. This shift in  $2\theta$ corresponds to an increase in ceria oxidation state and a decrease in oxygen nonstoichiometry  $(CeO_{2-\delta} \rightarrow CeO_2)$ . In addition, no apparent structure change was indentified for Cr (Fig. S11a), W (Fig. S11b) and In (Fig. S11c) catalysts after the subsequent nitrobenzene hydrogenation step at 25 and 100 °C, which is likely due to the kinetic limitations for H<sub>2</sub>O splitting and the subsequent nitrobenzene hydrogenation. This correlates well with the negligible activities as shown in Table S1 (entries 1-6) in which no nitrobenzene conversion was observed. Therefore, the XRD analysis illustrates the role of zero-valent metals or surface oxygen vacancies of metal oxide as the active redox sites and bulk sources of reducing potential for H2O dissociation and nitrobenzene hydrogenation. For comparison, the XRD patterns of ZnO, SnO<sub>2</sub>, Al<sub>2</sub>O<sub>3</sub> and TiO<sub>2</sub> catalysts before and after conventional hydrogenation of nitrobenzene using molecular hydrogen are also shown, indicating negligible structural change after the activity measurement (Fig. S12).

FT-IR measurements were employed to probe the surface interaction of nitrobenzene with the active site. Fig. 3c shows the IR spectra in the range of 1700-1200 cm<sup>-1</sup> at 25 °C, obtained upon the adsorption of nitrobenzene on Zn, ZnO, Sn and SnO<sub>2</sub>. The bands at 1530 cm<sup>-1</sup> and 1350 cm<sup>-1</sup> are assigned to the symmetric and asymmetric stretching of the nitro group (NO<sub>2</sub>), respectively. The phenyl ring vibration mode of nitrobenzene appears at 1480 cm<sup>-1</sup>. The adsorption of nitrobenzene resulted in a strong intensity over Zn and Sn, whereas a significantly lower adsorption intensity of nitrobenzene was observed over ZnO and SnO<sub>2</sub>. The strong adsorption of nitro group onto the surface of oxophilic Zn and Sn may contribute to their high catalytic activities.

Further insights on the mechanism of nitrobenzene reduction in H<sub>2</sub>O were monitored via *in situ* electron paramagnetic resonance (EPR) spectroscopy. The Zn system (black lines) and Sn system (red lines) started to show strong signals at 75 °C and 100 °C, respectively (Fig. S13). These radicals can be associated with the reduced intermediates such as N-phenylhydroxylamine radical species (–N• –OH) of nitrobenzene[11]. While ZnO<sub>2</sub> did not show evidence of radical species at any temperature. These results correspond well with the superior nitrobenzene hydrogenation performance of Zn and Sn catalysts in H<sub>2</sub>O.

The surface morphology and the microstructure changes of Zn, Sn, Al and Ti catalyst before and after ST/ECH of nitrobenzene were characterized with SEM. The initial Zn catalyst (Fig. 3d<sub>1</sub>, d<sub>2</sub>) was composed of small nanosized pyramid-like grains with relatively uniform diameters (50–100 nm). It's noteworthy that the pyramid-like grains of the spent catalysts, post nitrobenzene ST/ECH, transformed into conical stake-like crystals with increased size when the reaction temperature was elevated (Fig. 3d<sub>3</sub>-d<sub>6</sub>). The initial Sn catalyst (Fig. 3e<sub>1</sub>-e<sub>2</sub>) mainly consists of small particles of spherical morphology with relatively uniform diameters (50–100 nm), with no significant grain size growth observed after ST/ECH of nitrobenzene (Fig. 3e<sub>3</sub>-e<sub>6</sub>). The SEM

images for the spent Al and Ti were also investigated. The surface of Al (Fig. S14a-d) and Ti (Fig. S15a-d) were fairly smooth and composed of agglomerates with relatively non-uniform grains of 3-30 um for Al and above 30 um for Ti. A rough surface with steps and edges was observed for Al (Fig. S14c, d) and Ti (Fig. S15c, d) after reaction at 100 °C, which may be due to the partial oxidation of the metallic surface of Al and Ti when reacting with H<sub>2</sub>O, as confirmed by XRD analysis.

The elemental distribution of Zn, Sn, Al, and Ti catalysts before and after reaction were further characterized by STEM-EDX. For the initial Zn (Fig. 4a, a<sub>1</sub>-a<sub>3</sub>) and Sn (Fig. 4c, c<sub>1</sub>-c<sub>3</sub>) catalysts, a Zn rich (red) and Sn rich (red) region with O (green) preferably located near the surface were revealed (see Fig. S16b<sub>1</sub>-b<sub>3</sub> and Fig. S17b<sub>1</sub>-b<sub>3</sub> for further details). This observation, in combination with the XRD measurement, indicates that the initial Zn and Sn consisted of a mixture of metal and metal oxide. Energy-dispersive X-ray spectroscopy (EDX) mapping of the spent Zn (Fig. 4b<sub>1</sub>-b<sub>3</sub>) and Sn (Fig. 4d<sub>1</sub>-d<sub>3</sub>) catalysts demonstrate a homogeneously distribution of Zn (red), Sn (red) and O (green) elements throughout the samples, with tiny Sn rich regions remained (Fig. S16d<sub>1</sub>-d<sub>3</sub> and Fig. S17d<sub>1</sub>-d<sub>3</sub>). These results reveal that the metallic Zn and Sn were almost completely converted to zinc oxide (ZnO) and tin oxide (SnO and SnO<sub>2</sub>) after reaction at 150 °C. These are in good accordance with the XRD analysis. On the other hand, the initial Al (Fig. S18a, b<sub>1</sub>-b<sub>3</sub>) and Ti (Fig. S19a, b<sub>1</sub>-b<sub>3</sub>) catalysts are mainly composed of metallic phases. EDX mapping of Al (Fig. S18d<sub>1</sub>-d<sub>3</sub>) and Ti (Fig. S19d<sub>1</sub>-d<sub>3</sub>) catalysts revealed that the metallic Al and Ti regions

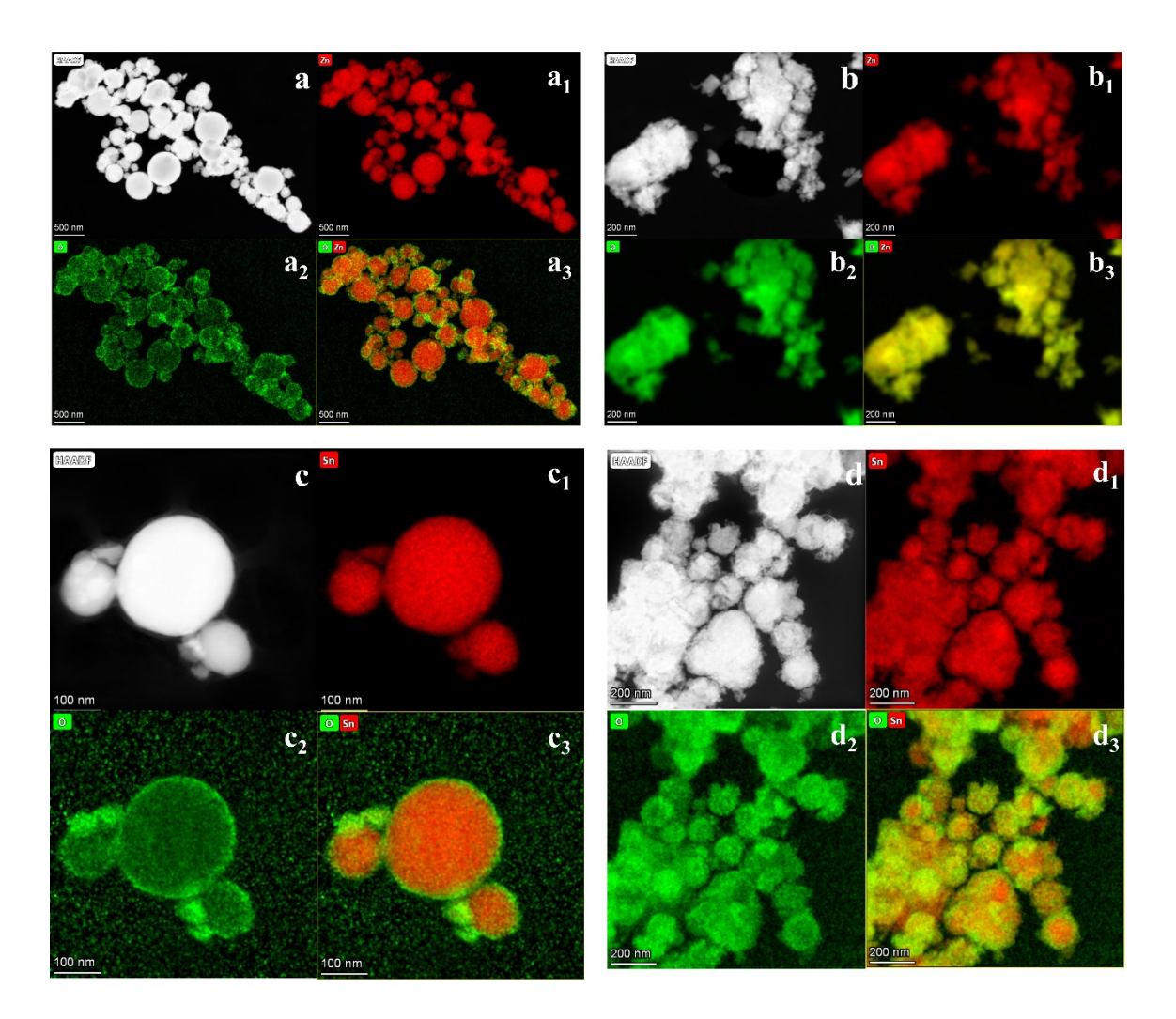
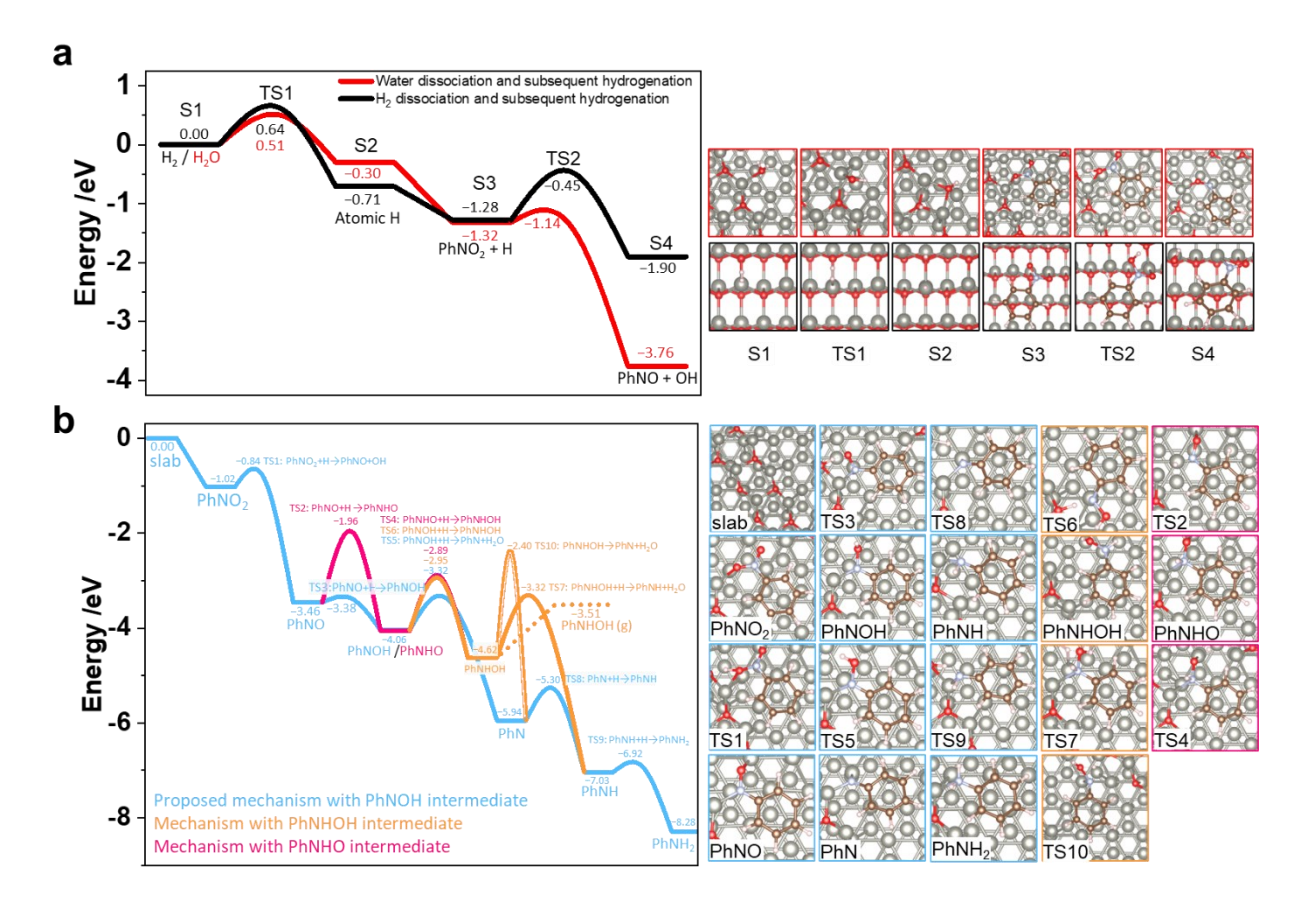


Fig. 4 (a) Representative STEM image and the corresponding element-mapping images of (a<sub>1</sub>) Zn, (a<sub>2</sub>) O and (a<sub>3</sub>) combination of Zn and O for the initial Zn catalyst. (b) Representative STEM image and the corresponding elemental-mapping images of (b<sub>1</sub>) Zn, (b<sub>2</sub>) O and (b<sub>3</sub>) combination of Zn and O for Zn catalyst after ST/ECH of nitrobenzene in H<sub>2</sub>O at 150 °C. (c) Representative STEM image and the corresponding element-mapping images of (c<sub>1</sub>) Sn, (c<sub>2</sub>) O and (c<sub>3</sub>) combination of Sn and O for the initial Sn catalyst. (d) Representative STEM image and the corresponding elemental-mapping images of (d<sub>1</sub>) Sn, (d<sub>2</sub>) O and (d<sub>3</sub>) combination of Sn and O for Sn catalyst after ST/ECH of nitrobenzene in H<sub>2</sub>O at 150 °C.

still dominate after reaction, suggesting that Al and Ti are only partially oxidized after ST/ECH of nitrobenzene. The above STEM-EDX mapping verified that Zn and Sn catalysts existed in the form of metallic Zn and Sn with oxide enrichment near the surface. The metallic phases are subsequently transformed into metal oxides after ST/ECH of nitrobenzene. While for Al and Ti, only very limited oxidation of metallic phases was observed after the reaction, which may be hindered by the high energy barriers for the metal cations migration through the oxide layers[66, 67].

**3.3 DFT Studies.** Density functional theory (DFT) calculations were performed to reveal the atomistic mechanisms of nitrobenzene hydrogenation reactions for Zn in water, and ZnO with molecular hydrogen. Consistent with the XRD and STEM-EDX characterizations, the structure model containing both Zn and ZnO phases were constructed and optimized to simulate the Zn catalyst for ST/ECH of nitrobenzene (see Fig. S20). As shown in Fig. 5a, the dissociation of H<sub>2</sub>O has a barrier of 0.51 eV over Zn with a reaction energy of -0.30 eV, demonstrating facile H<sub>2</sub>O dissociation and atomic H generation over metallic Zn. The barrier for H<sub>2</sub> dissociation on ZnO is 0.64 eV, which is comparably higher than that for H<sub>2</sub>O dissociation over the ZnO/Zn interface. (see detailed energy profiles in Fig. S21). The subsequent nitrobenzene hydrogenation sourcing H from H<sub>2</sub>O on ZnO/Zn is -2.44 eV exergonic, with an energy barrier of 0.18 eV. In comparison, the corresponding hydrogenation step for conventional hydrogenation using molecular H<sub>2</sub> over ZnO is only -0.62 eV exergonic and kinetically hindered with a barrier of 0.83 eV. Additionally, in agreement with the FT-IR characterization, the nitrobenzene binds 0.45 eV more strongly on Zn/ZnO interface than on ZnO (Table S5). To summarize, these results indicate (i) strong absorption of nitrobenzene; (ii) facile generation of atomic H through H<sub>2</sub>O dissociation on ZnO/Zn interface; and (iii) the resulting atomic H is active for nitrobenzene hydrogenation. These results



**Fig. 5** (a) Energy profile of H production through H<sub>2</sub>O/H<sub>2</sub> dissociation and the subsequent nitrobenzene hydrogenation by the produced H. Red line indicates water dissociation on ZnO/Zn structure while black line indicates the H<sub>2</sub> dissociation on ZnO structure. The structures of corresponding states are given on the right; transition states are termed as "TS". (b) Energy profile of nitrobenzene hydrogenation to aniline. Proposed and other possible mechanisms are outlined by different color. See main text for detail information. Colour code for the structures: Zn (grey), O (red), C (brown), H (pink). Energy unit in eV.

corroborate well with the superior hydrogenation performance of the Zn catalyst. In contrast, hydrogenation of nitrobenzene over ZnO with molecular H<sub>2</sub> is impeded by the high energy barrier and low H<sub>2</sub> solubility.

In addition to the high activity of Zn, it is quite remarkable that the relatively large Zn particles can be fully oxidized to ZnO during the reaction. Nakamura et al.[68] and Hartley et al.[69] investigated the oxidation behavior of Zn nanoparticles in air, H<sub>2</sub>O and CO<sub>2</sub>, which demonstrated the oxidation through outward diffusion of Zn across ZnO film by transmission electron microscopy. Similarly, Jeurgens et al.[66] studied the growth kinetic and mechanisms of aluminum-oxide films by *in-situ* X-ray photoelectron spectroscopy, indicating that the oxide-film growth rate is realized by interstitial, outward migration of Al cations. A value of 2.6 eV was determined for the rate-limiting energy barrier for Al cation motion. Our DFT calculation indicates a 0.86-1.00 eV energy barrier for the migration of Zn through cation vacancies in ZnO (Fig. S22a). This confirms that Zn can be oxidized to ZnO through outwards diffusion of Zn cations. For comparison, the diffusion of Al and Ti atoms are largely hindered in their corresponding oxides, with barrier ranges of 1.8-2.0 eV and 1.6-2.2 eV, respectively (Fig. S22b and c). These results are consistent with the fact that the metallic Zn was almost completely converted to ZnO, whereas only partial oxidation of Al and Ti were observed after reaction at 150 °C.

The detailed reaction pathways for nitrobenzene hydrogenation to aniline over the Zn catalyst are shown in Fig. 5b. First, the energetically more favorable pathway is depicted. An O atom in nitrobenzene (PhNO<sub>2</sub>) is hydrogenated by an H atom with an energy barrier of 0.18 eV. The product is quite unstable, and it decomposes to nitrosobenzene (PhNO) and OH. Thus, we only considered the further hydrogenation based on PhNO and neglected the possibility of other species and mechanisms[70-72]. PhNO can be hydrogenated at both N and O sites. The hydrogenation of PhNO to PhNOH at O atom is more favorable with a barrier of 0.08 eV (blue line). For the PhNOH species, two hydrogenation pathways were identified. The hydrogenation at O atom is preferable exothermic by 1.90 eV with a barrier of 0.74 eV, producing PhN and H<sub>2</sub>O (blue line). The PhN

will be hydrogenated sequentially with a low barrier of 0.11 eV, resulting in the final hydrogenation product aniline (PhNH<sub>2</sub>).

Other possible hydrogenation pathways are also illustrated. For example, PhNO can be hydrogenated to PhNHO at N position with a barrier of 1.50 eV (pink line) and TS2 as transition state (TS). Although the hydrogenation product PhNHO is calculated to have a close energy with respect to PhNOH when they adsorb at the surface, the formation of PhNHO is kinetically unfavorable relative to PhNOH, and the hydrogenation of PhNHO to N-Phenylhydroxylamine (PhNHOH) also has a high barrier of 1.16 eV when H attacks the N atom (TS4). These high barriers make the pathways less favorable. The PhNHOH can also be generated from the hydrogenation of PhNOH with similar barrier of PhNHO hydrogenation. PhNHOH can desorb from surface with a desorption energy of 1.11 eV (dash orange line) instead of further hydrogenation (TS7) with barrier of 1.3 eV or intramolecular dehydration (TS10) with an even larger barrier (2.22 eV). These results indicate that PhNHOH can be expected as a partially hydrogenated byproduct from the process. Higher reaction temperatures would disproportionally favor the further hydrogenation of PhNHOH relative to its desorption, and hence higher selectivity towards PhNH<sub>2</sub> can be expected. These results are in line with experimental observations that the selectivity of PhNHOH decreased with increasing the reaction temperature.

#### 4. Conclusion

To summarize, we have proposed and demonstrated an environmentally benign and efficient solar thermochemical/electrochemical hydrogenation (ST/ECH) route for the reduction of nitroarenes, a family of reactions with high practical significance. The ST/ECH process eliminates the use of noble metal catalysts, molecular H<sub>2</sub>, and organic hydrogen donors, offering the potential to harness

renewable energy sources such as solar irradiation or renewable electricity. 14 oxophilic zero-valent metals as well as reduced CeO<sub>2</sub> were investigated as prototype catalysts/water-splitting agents to determine the feasibility of this process. Zn and Sn displayed excellent performance for the reduction of a wide range of organic nitro compounds at ambient temperature and pressure, with H<sub>2</sub> utilization efficiencies that are 1-2 orders of magnitude higher than state-of-the-art catalytic hydrogenation processes. Mechanistic investigations indicate that oxophilic zero-valent metals or surface oxygen vacancies act as the active redox centers for nitrobenzene adsorption and *in-situ* generation of H atoms from H<sub>2</sub>O. The *in-situ* generated H atoms play a crucial role for the highly effective reductive transformation, eliminating the barriers for H<sub>2</sub> dissolution in the reaction medium and the subsequent dissociation on the catalyst surface. Based on the generalizability observed experimentally, the ST/ECH concept can potentially be applied towards a wide range of hydrogenation and reductive reactions. This can open new avenues for the storage of renewable energy through a myriad of organic transformations.

## Acknowledgements

This work was supported by the U.S. National Science Foundation (Award No. CBET-2116724 and CBET-1923468) and the Kenan Institute for Engineering, Technology and Science at North Carolina State University. We acknowledge the computing resources provided by North Carolina State University High Performance Computing Services Core Facility (RRID: SCR\_022168). The STEM-EDX was performed in part at the Analytical Instrumentation Facility (AIF) at North Carolina State University, which is supported by the State of North Carolina and the National Science Foundation (Award No. ECCS-1542015). This work made use of instrumentation at AIF acquired with support from the National

Science Foundation (DMR-1726294). The AIF is a member of the North Carolina Research Triangle Nanotechnology Network (RTNN), a site in the National Nanotechnology Coordinated Infrastructure (NNCI).

# **Competing interests**

The authors declare no competing interest.

### **Additional information**

Supplementary information is available in the online version of the paper.

#### REFERENCES

- [1] N. Ono, The Nitro Group in Organic Synthesis, Wiley-VCH, (2001).
- [2] H. Feuer, Nitrile Oxides Nitrones and Nitronates in Organic Synthesis, John Wiley, (2008).
- [3] F.A. Westerhaus, R.V. Jagadeesh, G. Wienhofer, M.M. Pohl, J. Radnik, A.E. Surkus, J. Rabeah, K. Junge, H. Junge, M. Nielsen, A. Bruckner, M. Beller, Heterogenized cobalt oxide catalysts for nitroarene reduction by pyrolysis of molecularly defined complexes, Nat. Chem., 5 (2013) 537-543.
- [4] A. Corma, P. Serna, Chemoselective hydrogenation of nitro compounds with supported gold catalysts, Science, 313 (2006) 332-334.
- [5] A. Grirrane, A. Corma, H. Garcia, Gold-Catalyzed Synthesis of Aromatic Azo Compounds from Anilines and Nitroaromatics, Science, 322 (2008) 1661-1664.
- [6] S. Zhang, C.R. Chang, Z.Q. Huang, J. Li, Z. Wu, Y. Ma, Z. Zhang, Y. Wang, Y. Qu, High Catalytic Activity and Chemoselectivity of Sub-nanometric Pd Clusters on Porous Nanorods of CeO2 for Hydrogenation of Nitroarenes, J. Am. Chem. Soc., 138 (2016) 2629-2637.
- [7] L. Lin, S. Yao, R. Gao, X. Liang, Q. Yu, Y. Deng, J. Liu, M. Peng, Z. Jiang, S. Li, Y.W. Li, X.D. Wen, W. Zhou, D. Ma, A highly CO-tolerant atomically dispersed Pt catalyst for chemoselective hydrogenation, Nat Nanotechnol, 14 (2019) 354-361.
- [8] G. Chen, C. Xu, X. Huang, J. Ye, L. Gu, G. Li, Z. Tang, B. Wu, H. Yang, Z. Zhao, Z. Zhou, G. Fu, N. Zheng, Interfacial electronic effects control the reaction selectivity of platinum catalysts, Nat. Mater., 15 (2016) 564-569.
- [9] A. Corma, P. Serna, P. Concepcion, J.J. Calvino, Transforming nonselective into chemoselective metal catalysts for the hydrogenation of substituted nitroaromatics, J. Am. Chem. Soc., 130 (2008) 8748-8753.
- [10] C.L. YOUNG, International Union of Pure and Applied Chemistry, (1981).
- [11] A. Cheruvathoor Poulose, G. Zoppellaro, I. Konidakis, E. Serpetzoglou, E. Stratakis, O. Tomanec, M. Beller, A. Bakandritsos, R. Zboril, Fast and selective reduction of nitroarenes under visible light with an earth-abundant plasmonic photocatalyst, Nat Nanotechnol, 17 (2022) 485-492.
- [12] C. Zhang, J. Lu, M. Li, Y. Wang, Z. Zhang, H. Chen, F. Wang, Transfer hydrogenation of nitroarenes with hydrazine at near-room temperature catalysed by a MoO2 catalyst, Green Chemistry, 18 (2016) 2435-2442.
- [13] G. Wienhofer, I. Sorribes, A. Boddien, F. Westerhaus, K. Junge, H. Junge, R. Llusar, M. Beller, General and selective iron-catalyzed transfer hydrogenation of nitroarenes without base, J. Am. Chem. Soc., 133 (2011) 12875-12879.
- [14] I. Sorribes, G. Wienhofer, C. Vicent, K. Junge, R. Llusar, M. Beller, Chemoselective transfer hydrogenation to nitroarenes mediated by cubane-type Mo3S4 cluster catalysts, Angew. Chem., Int. Ed., 51 (2012) 7794-7798.
- [15] S. Doherty, J.G. Knight, T. Backhouse, A. Bradford, F. Saunders, R.A. Bourne, T.W. Chamberlain, R. Stones, A. Clayton, K. Lovelock, Highly efficient aqueous phase reduction of nitroarenes catalyzed by phosphine-decorated polymer immobilized ionic liquid stabilized PdNPs, Catalysis Science & Technology, 8 (2018) 1454-1467.
- [16] H. Göksu, S.F. Ho, Ö. Metin, K. Korkmaz, A. Mendoza Garcia, M.S. Gültekin, S. Sun, Tandem Dehydrogenation of Ammonia Borane and Hydrogenation of Nitro/Nitrile Compounds Catalyzed by Graphene-Supported NiPd Alloy Nanoparticles, ACS Catal., 4 (2014) 1777-1782.

- [17] Q. Yang, Y.Z. Chen, Z.U. Wang, Q. Xu, H.L. Jiang, One-pot tandem catalysis over Pd@MIL-101: boosting the efficiency of nitro compound hydrogenation by coupling with ammonia borane dehydrogenation, Chem Commun (Camb), 51 (2015) 10419-10422.
- [18] C. Yu, J. Fu, M. Muzzio, T. Shen, D. Su, J. Zhu, S. Sun, CuNi Nanoparticles Assembled on Graphene for Catalytic Methanolysis of Ammonia Borane and Hydrogenation of Nitro/Nitrile Compounds, Chem. Mater., 29 (2017) 1413-1418.
- [19] F. Wang, O. Planas, J. Cornella, Bi(I)-Catalyzed Transfer-Hydrogenation with Ammonia-Borane, J. Am. Chem. Soc., 141 (2019) 4235-4240.
- [20] K. Junge, B. Wendt, N. Shaikh, M. Beller, Iron-catalyzed selective reduction of nitroarenes to anilines using organosilanes, Chem Commun (Camb), 46 (2010) 1769-1771.
- [21] W.C. Chueh, C. Falter, M. Abbott, D. Scipio, P. Furler, S.M. Haile, A. Steinfeld, High-flux solar-driven thermochemical dissociation of CO2 and H2O using nonstoichiometric ceria, Science, 330 (2010) 1797-1801.
- [22] C.L. Muhich, B.W. Evanko, K.C. Weston, P. Lichty, X. Liang, J. Martinek, C.B. Musgrave, A.W. Weimer, Efficient generation of H<sub>2</sub> by splitting water with an isothermal redox cycle, Science, 341 (2013) 540-542.
- [23] C.L. Muhich, B.D. Ehrhart, V.A. Witte, S.L. Miller, E.N. Coker, C.B. Musgrave, A.W. Weimer, Predicting the solar thermochemical water splitting ability and reaction mechanism of metal oxides: a case study of the hercynite family of water splitting cycles, Energy Environ. Sci., 8 (2015) 3687-3699.
- [24] K.J. Warren, J.T. Tran, A.W. Weimer, A thermochemical study of iron aluminate-based materials: a preferred class for isothermal water splitting, Energy Environ. Sci., 15 (2022) 806-821.
- [25] D. R. Barcellos, M.D. Sanders, J. Tong, A.H. McDaniel, R.P. O'Hayre, BaCe0.25Mn0.75O3–δ—a promising perovskite-type oxide for solar thermochemical hydrogen production, Energy Environ. Sci., (2018).
- [26] M. Roeb, C. Sattler, Isothermal water splitting, Science, 341 (2013) 470-471.
- [27] J.A. Herron, J. Kim, A.A. Upadhye, G.W. Huber, C.T. Maravelias, A general framework for the assessment of solar fuel technologies, Energy Environ. Sci., 8 (2015) 126-157.
- [28] E.A. Fletcher, R.L. Moen, Hydrogen and Oxygen from Water, Science, 197 (1977) 1050-1056.
- [29] C. Etievant, Solar high-temperature direct water splitting a review of experiments in France Solar Energy Materials, 24 (1991) 413-440.
- [30] W.C. Chueh, F. C., Abbott M., S. D., F. P., S.M. Haile, A. Steinfeld, High-Flux Solar-Driven Thermochemical Dissociation of CO<sub>2</sub> and H<sub>2</sub>O Using Nonstoichiometric Ceria, Science, 330 (2010) 1797-1801.
- [31] M. Tou, R. Michalsky, A. Steinfeld, Solar-Driven Thermochemical Splitting of CO<sub>2</sub> and In Situ Separation of CO and O<sub>2</sub> across a Ceria Redox Membrane Reactor, Joule, (2017) 146-154.
- [32] D. Marxer, P. Furler, M. Takacs, A. Steinfeld, Solar thermochemical splitting of CO<sub>2</sub> into separate streams of CO and O<sub>2</sub> with high selectivity, stability, conversion, and efficiency, Energy Environ. Sci., 10 (2017) 1142-1149.
- [33] P. Furler, J.R. Scheffe, A. Steinfeld, Syngas production by simultaneous splitting of H<sub>2</sub>O and CO<sub>2</sub> via ceria redox reactions in a high-temperature solar reactor, Energy Environ. Sci., 5 (2012) 6098-6103.
- [34] R. Schappi, D. Rutz, F. Dahler, A. Muroyama, P. Haueter, J. Lilliestam, A. Patt, P. Furler, A. Steinfeld, Drop-in fuels from sunlight and air, Nature, 601 (2022) 63-68.

- [35] C. Ruan, R. Akutsu, K. Yang, N.M. Zayan, J. Dou, J. Liu, A. Bose, L. Brody, H.H. Lamb, F. Li, Hydrogenation of bio-oil-derived oxygenates at ambient conditions via a two-step redox cycle, Cell Reports Physical Science, 4 (2023) 101506.
- [36] P. Krenzke, K. Krueger, N. Leonard, S. Duncan, R.D. Palumbo, S. Möller, A Solar Thermal Electrolytic Reactor for Studying the Production of Metals From Their Oxides, Journal of Solar Energy Engineering, 132 (2010).
- [37] E. Koepf, W. Villasmil, A. Meier, Pilot-scale solar reactor operation and characterization for fuel production via the Zn/ZnO thermochemical cycle, Applied Energy, 165 (2016) 1004-1023.
- [38] A.J. Carrillo, A.H. Bork, T. Moser, E. Sediva, Z.D. Hood, J.L.M. Rupp, Modifying La<sub>0.6</sub>Sr<sub>0.4</sub>MnO<sub>3</sub> Perovskites with Cr Incorporation for Fast Isothermal CO<sub>2</sub>-Splitting Kinetics in Solar-Driven Thermochemical Cycles, Advanced Energy Materials, (2019) 1803886.
- [39] X. Zhu, Q. Imtiaz, F. Donat, C.R. Müller, F. Li, Chemical looping beyond combustion a perspective, Energy Environ. Sci., (2020).
- [40] X. Wang, Y. Gao, E. Krzystowczyk, S. Iftikhar, J. Dou, R. Cai, H. Wang, C. Ruan, S. Ye, F. Li, High-throughput oxygen chemical potential engineering of perovskite oxides for chemical looping applications, Energy Environ. Sci., 15 (2022) 1512-1528.
- [41] I.S. Metcalfe, B. Ray, C. Dejoie, W. Hu, C. de Leeuwe, C. Dueso, F.R. Garcia-Garcia, C.M. Mak, E.I. Papaioannou, C.R. Thompson, J.S.O. Evans, Overcoming chemical equilibrium limitations using a thermodynamically reversible chemical reactor, Nat. Chem., 11 (2019) 638-643.
- [42] C. Ruan, X. Wang, C. Wang, L. Zheng, L. Li, J. Lin, X. Liu, F. Li, X. Wang, Selective catalytic oxidation of ammonia to nitric oxide via chemical looping, Nature Communications, 13 (2022).
- [43] G. Kresse, J. Furthmüller, Efficient iterative schemes for ab initio total-energy calculations using a plane-wave basis set, Phys. Rev. B, 54 (1996) 11169-11186.
- [44] P.E. Blöchl, Projector augmented-wave method, Phys. Rev. B, 50 (1994) 17953-17979.
- [45] J.P. Perdew, K. Burke, M. Ernzerhof, Generalized Gradient Approximation Made Simple, Phys. Rev. Lett., 77 (1996) 3865-3868.
- [46] G. Henkelman, B.P. Uberuaga, H. Jónsson, A climbing image nudged elastic band method for finding saddle points and minimum energy paths, J. Chem. Phys., 113 (2000) 9901-9904.
- [47] K. Yang, J. Liu, B. Yang, Mechanism and Active Species in NH3 Dehydrogenation under an Electrochemical Environment: An Ab Initio Molecular Dynamics Study, ACS Catal., 11 (2021) 4310-4318.
- [48] K. Yang, J. Liu, B. Yang, Electrocatalytic oxidation of ammonia on Pt: Mechanistic insights into the formation of N2 in alkaline media, J. Catal., 405 (2022) 626-633.
- [49] K. Mathew, R. Sundararaman, K. Letchworth-Weaver, T.A. Arias, R.G. Hennig, Implicit solvation model for density-functional study of nanocrystal surfaces and reaction pathways, J. Chem. Phys., 140 (2014) 084106.
- [50] H. Jin, P. Li, P. Cui, J. Shi, W. Zhou, X. Yu, W. Song, C. Cao, Unprecedentedly high activity and selectivity for hydrogenation of nitroarenes with single atomic Co(1)-N(3)P(1) sites, Nat Commun, 13 (2022) 723.
- [51] X. Long, Z. Li, G. Gao, P. Sun, J. Wang, B. Zhang, J. Zhong, Z. Jiang, F. Li, Graphitic phosphorus coordinated single Fe atoms for hydrogenative transformations, Nat Commun, 11 (2020) 4074.

- [52] G. Zhang, F. Tang, X. Wang, L. Wang, Y.-N. Liu, Atomically Dispersed Co–S–N Active Sites Anchored on Hierarchically Porous Carbon for Efficient Catalytic Hydrogenation of Nitro Compounds, ACS Catal., (2022) 5786-5794.
- [53] Z. Wei, J. Wang, S. Mao, D. Su, H. Jin, Y. Wang, F. Xu, H. Li, Y. Wang, In Situ-Generated Co0-Co3O4/N-Doped Carbon Nanotubes Hybrids as Efficient and Chemoselective Catalysts for Hydrogenation of Nitroarenes, ACS Catal., 5 (2015) 4783-4789.
- [54] P. Zhou, L. Jiang, F. Wang, K.J. Deng, K.L. Lv, Z.H. Zhang, High performance of a cobalt-nitrogen complex for the reduction and reductive coupling of nitro compounds into amines and their derivatives, Science Advances, 3 (2017).
- [55] X. Shi, X. Wang, X. Shang, X. Zou, W. Ding, X. Lu, High Performance and Active Sites of a Ceria-Supported Palladium Catalyst for Solvent-Free Chemoselective Hydrogenation of Nitroarenes, ChemCatChem, 9 (2017) 3743-3751.
- [56] W. Li, X. Cui, K. Junge, A.-E. Surkus, C. Kreyenschulte, S. Bartling, M. Beller, General and Chemoselective Copper Oxide Catalysts for Hydrogenation Reactions, ACS Catal., 9 (2019) 4302-4307
- [57] P. Ryabchuk, G. Agostini, M.M. Pohl, H. Lund, A. Agapova, H. Junge, K. Junge, M. Beller, Intermetallic nickel silicide nanocatalyst-A non-noble metal-based general hydrogenation catalyst, Science Advances, 4 (2018).
- [58] R.V. Jagadeesh, A.E. Surkus, H. Junge, M.M. Pohl, J. Radnik, J. Rabeah, H.M. Huan, V. Schunemann, A. Bruckner, M. Beller, Nanoscale Fe2O3-Based Catalysts for Selective Hydrogenation of Nitroarenes to Anilines, Science, 342 (2013) 1073-1076.
- [59] L. Zhu, H. Zhang, H. Zhu, H. Fu, A. Kroner, Z. Yang, H. Ye, B.H. Chen, R. Luque, Controlling nanostructures of PtNiCo/C trimetallic nanocatalysts and relationship of structure-catalytic performance for selective hydrogenation of nitroarenes, Journal of Catalysis, 413 (2022) 978-991.
- [60] Y. Zhang, J. Zhou, Synergistic catalysis by a hybrid nanostructure Pt catalyst for high-efficiency selective hydrogenation of nitroarenes, Journal of Catalysis, 395 (2021) 445-456.
- [61] T.N. Ye, Y. Lu, J. Li, T. Nakao, H. Yang, T. Tada, M. Kitano, H. Hosono, Copper-Based Intermetallic Electride Catalyst for Chemoselective Hydrogenation Reactions, J. Am. Chem. Soc., 139 (2017) 17089-17097.
- [62] I. Sorribes, L. Liu, A. Corma, Nanolayered Co–Mo–S Catalysts for the Chemoselective Hydrogenation of Nitroarenes, ACS Catal., 7 (2017) 2698-2708.
- [63] M.B. Gawande, A.K. Rathi, J. Tucek, K. Safarova, N. Bundaleski, O.M.N.D. Teodoro, L. Kvitek, R.S. Varma, R. Zboril, Magnetic gold nanocatalyst (nanocat-Fe–Au): catalytic applications for the oxidative esterification and hydrogen transfer reactions, Green Chem., 16 (2014) 4137-4143.
- [64] F.M. Geilen, B. Engendahl, M. Holscher, J. Klankermayer, W. Leitner, Selective homogeneous hydrogenation of biogenic carboxylic acids with [Ru(TriPhos)H]+: a mechanistic study, J. Am. Chem. Soc., 133 (2011) 14349-14358.
- [65] H. Jin, P. Li, P. Cui, J. Shi, W. Zhou, X. Yu, W. Song, C. Cao, Unprecedentedly high activity and selectivity for hydrogenation of nitroarenes with single atomic Co1-N3P1 sites, Nat Commun, 13 (2022) 723.
- [66] L.P.H. Jeurgens, W.G. Sloof, F.D. Tichelaar, E.J. Mittemeijer, Growth kinetics and mechanisms of aluminum-oxide films formed by thermal oxidation of aluminum, J. Appl. Phys., 92 (2002) 1649-1656.

- [67] L. Nguyen, T. Hashimoto, D.N. Zakharov, E.A. Stach, A.P. Rooney, B. Berkels, G.E. Thompson, S.J. Haigh, T.L. Burnett, Atomic-Scale Insights into the Oxidation of Aluminum, ACS Appl. Mater. Interfaces, 10 (2018) 2230-2235.
- [68] R. Nakamura, J.G. Lee, D. Tokozakura, H. Mori, H. Nakajima, Formation of hollow ZnO through low-temperature oxidation of Zn nanoparticles, Materials Letters, 61 (2007) 1060-1063.
- [69] V. Tongnan, T. Sornchamni, N. Laosiripojana, U.W. Hartley, Study of crystal growth and kinetic parameters of Zn/ZnO oxidation in the presence of H2O and CO2, Reaction Kinetics, Mechanisms and Catalysis, 125 (2018) 99-110.
- [70] H. Wang, W. Zhang, Y. Liu, M. Pu, M. Lei, First-Principles Study on the Mechanism of Nitrobenzene Reduction to Aniline Catalyzed by a N-Doped Carbon-Supported Cobalt Single-Atom Catalyst, J. Phys. Chem. C, 125 (2021) 19171-19182.
- [71] H. Wang, C. Yue, J. Du, M. Pu, M. Lei, First Principles Study on the Mechanism of Nitrobenzene Hydrogenation by a Ni1/CeO2-x(111) Single-Atom Catalyst, J. Phys. Chem. C, 127 (2023) 16880-16890.
- [72] T. He, C. Zhang, L. Zhang, A. Du, Single Pt atom decorated graphitic carbon nitride as an efficient photocatalyst for the hydrogenation of nitrobenzene into aniline, Nano Research, 12 (2019) 1817-1823.